Construction of novel Ru-embedded bulk g-C$_3$N$_4$ photocatalysts toward efficient and sustainable photocatalytic hydrogen production

Mohammed Ismael

Institute of Chemistry, Technical Chemistry, Carl von Ossietzky University Oldenburg, Carl-von-Ossietzky-Str. 9-11, 26129 Oldenburg, Germany
Leibniz University Hannover, Institute of Electric Power Systems, 30167 Hannover, Germany

A B S T R A C T

Novel Ru-embedded bulk graphitic carbon nitride (g-C$_3$N$_4$) photocatalysts containing different wt% of Ru (0.5–2 % wt) were synthesized by a simple mixing method of ruthenium complex with g-C$_3$N$_4$. The photocatalytic activity of the synthesized photocatalysts was assessed for hydrogen production in an aqueous solution containing methanol with and without Pt. The optimal hydrogen production rate of the most active photocatalyst (0.8 % Ru/CN) was 246 μmol/h without Pt and 1021 μmol/h with Pt, which was more than two times higher than pure g-C$_3$N$_4$. Various physiochemical techniques such as X-ray diffraction (XRD), N$_2$ adsorption-desorption isotherms, transmission electron microscopy (TEM), X-ray photoelectron spectroscopy (XPS), UV–vis diffuse reflectance spectroscopy (UV–vis DRS), photoluminescence spectroscopy (PL) and transition photocurrent response (PC) were applied to investigate the origin of activity of the Ru$_x$/CN photocatalysts. Results indicated that the loading of g-C$_3$N$_4$ with Ru nanoparticles enlarged its surface area and enhanced visible light absorption. Importantly, Ru nanoparticles promoted the charge carrier separation and transfer efficiency of g-C$_3$N$_4$ revealed by the PL and PC measurements, enhancing the photocatalytic activity of the embedded photocatalyst. Furthermore, XPS proved the existence of Ru (II) of RuO$_2$ and metallic Ru^0. The Ru-embedded g-C$_3$N$_4$ showed high photocatalytic activity, which makes them attractive materials for further applications in photocatalysis.

1. Introduction

Environmental pollution, rising CO$_2$ levels in the atmosphere, and energy shortages are quickly turning into serious issues for human society. To overcome these two issues, scientists have been compelled to create a clean, renewable energy source that may supplant fossil fuels as the primary source of energy for the entire world. Given its reputation as a clean and sustainable energy source and zero-emission, hydrogen has the potential to reduce the use of harmful fossil fuels in transportation [1]. The conventional method of producing hydrogen from fossil fuels is well advanced, but it consumes a lot of energy and produces a lot of CO$_2$ which contributes to the greenhouse effect. For that, photocatalysis technology using solar energy and water is an ideal and promising method for efficient hydrogen production [2,3]. The benefits of this approach include the fact that solar energy is limitless and that the photocatalytic hydrogen products are clean. In this context, many researchers concur that water photolysis can transform solar energy into pure hydrogen energy, providing a long-term and viable solution to the energy crisis and environmental issues. Since photocatalytic materials are the core of photocatalytic technology, a multitude of photocatalytic

materials have been explored as candidates for photocatalytic water splitting, but only a few of these materials have great attention [4–8]. Among them, graphitic carbon nitride (g-C$_3$N$_4$) as a non-metallic organic photocatalytic material has become one of the hot spots in photocatalytic hydrogen production owing to its abundance, inexpensive, physiochemical stability, suitable bandgap energy (2.7 eV), and appropriate banding width [9–12]. As a graphene-like n-type semiconductor, g-C$_3$N$_4$ can be easily prepared on a large scale using thermal condensation from available and cheap nitrogen-containing precursors [13–15]. These properties induce g-C$_3$N$_4$ to show good performance in various photocatalytic reactions, including CO$_2$ photoreduction [16], hydrogen production [17,18], organic pollutants degradation [19,20], organic transformation [21,22], and N$_2$ fixation [23,24]. However, the photocatalytic activity of pristine g-C$_3$N$_4$ is still limited due to its restricted visible-light harvesting capacity in the long-wavelength region, poor electrical response, high degree of copolymerization, high recombination of photogenerated charge carriers, and low surface area [25,26].

Thus far, several routes have been developed to enhance the photocatalytic activity of g-C$_3$N$_4$, such as designing mesoporous structure

[27,28], exfoliation to nanosheets [29,30], elemental loading [31,32], dye sensitization [33,34], and coupling with other semiconductors [35,36]. Among all these strategies, anchoring or coupling metal ions onto g-C$_3$N$_4$ has emerged attractive attention because it enhances solar energy conversion by narrowing the bandgap energy, extends the light response toward a longer wavelength (visible region), and creates more surface-active sites [37,38]. Additionally, the six nitrogen lone-pair electrons in the g-C$_3$N$_4$ nitrogen tank make it simple to form ion-dipole interactions with the cations that are added to the tank for ion loading to enhance its energy band and electronic structure [39,40]. Thus, loading of g-C$_3$N$_4$ with precious metals such as Pt [41], Au [42], or non-precious metals like Cu [43] or Zn [44] has been found not only to play a major role in changing the electronic properties of g-C$_3$N$_4$ but also to improve the whole photocatalytic performance of the photocatalyst.

Recently, ruthenium (mainly Ru (III)) has been explored as a Pt substitute due to its many advantages, including low cost, excellent stability, and potential for electron trapping and transport [45]. Due to its excellent activity, selectivity, and stability properties, Ru (III) has been widely utilized in thermal catalytic CO$_2$ reforming of CH$_4$, Fischer-Tropsch synthesis, and CO$_2$ methanation [46]. Ruthenium (Ru) can efficiently shift the absorption edge of the semiconductor toward the visible region arising from the creation of an intermediate energy level of the semiconductor [47,48]. Similarly, Ru (II) complex-based dyes sensitized g-C$_3$N$_4$ were tested under visible light and observed enhanced hydrogen evolution rate due to faster charge carrier separation [49]. However, there aren't many publications on the usage of Ru^x as a co-catalyst for photocatalytic hydrogen generation applications. For instance, Wang et al. [50] successfully synthesized ruthenium phosphide/C$_3$N$_4$ composites via in situ-growth method for determining the hydrogen production activity. Their findings revealed that 0.1%RP/ C$_3$N$_4$ exhibited the highest activity (2110 μmol/h g^{-1}). Besides, the photocatalytic activities of Ru/g-C$_3$N$_4$ photocatalyst in ammonia borane reactions were also reported. In that case, Garcia et al. [51] prepared Ru/C/g-C$_3$N$_4$ photocatalysts by a conventional impregnation method, which demonstrated enhanced ammonia borane dehydrogenation reaction under dark and visible light irradiation conditions. They attributed the developed photocatalytic to enhancing the optical properties of the Ru/C/g-C$_3$N$_4$ photocatalyst arising from the presence of both C and Ru. Similarly, Li et al. used Ru/porous g-C$_3$N$_4$ photocatalysts to produce H$_2$ from ammonia borane hydrolysis with NaOH and various NH$_4$Cl doses [52]. They also produced Ru/porous g-C$_3$N$_4$ photocatalysts from melamine and NH$_4$Cl using a simple adsorption-in situ reduction technique. Their findings showed that a 1 (melamine): 3 (NH$_4$Cl) ratio is ideal and exhibits the highest hydrogen production activity, which was attributed to the porous structure's role in increasing the reactants' surface-active sites and diffusion channels as well as the role of Ru metal in improving the photocatalytic activity. Ru/g-C$_3$N$_4$ can also be used as a heterogeneous catalyst, the work of Sharma et al. [53] for example, demonstrated that a Ru/g-C$_3$N$_4$ photocatalyst was successfully achieved by simple mixing of g-C$_3$N$_4$ and RuCl$_3$ in an ethanol solution, showing highly effective visible-light performance for selective transfer hydrogenation of nitroarenes and olefins in the presence of hydrazine. The conjugated structure of g-C$_3$N$_4$ and the addition of ruthenium, which acts as an improved active semiconductor, were thought to be responsible for the greater activity of the Ru/g-C$_3$N$_4$ photocatalysts. Also, Ru/ g-C$_3$N$_4$ photocatalyst can be applied in alcohol oxidation, hydrogen transfer reactions of aldehyde and ketones [54,55] and for visible-light CO$_2$ photoreduction [56,57]. To the best of our knowledge, no research has previously been done on the influence of Ru (III) on the bulk g-C$_3$N$_4$ photocatalyst for photocatalytic H$_2$ production. Herein we for the first time report a simple, and environmentally friendly method to synthesize novel Ru-embedded g-C$_3$N$_4$ photocatalyst using [Ru(bpy)$_2$Cl$_2$]$^+$ and melamine as precursors for ruthenium and g-C$_3$N$_4$, respectively. The photocatalytic activity was assessed for hydrogen production with and without Pt. Several experimental studies were performed to investigate the origin of the high-activity performance of the as-synthesized

photocatalysts.

2. Experimental

2.1. Synthesis of [Ru(bpy)$_2$Cl$_2$]$^+$ [58]

All chemicals used in this work were analytical grade and were used without further treatment. 2,2-Bipyridine (2.34 g, 15 mmol), ruthenium chloride trihydrate RuCl$_3$•3H$_2$O (1.95 g, 7.45 mmol), and lithium chloride (2.1 g, 50 mmol) were dissolved in DMF (20 mL) and refluxed for 8 h. After allowing the reaction mixture to settle to ambient temperature, 125 mL of acetone was gradually added. The resulting mixture was refrigerated for 12 h at 0 °C. A membrane filter was used to filter the separated product while it was under vacuum. To eliminate contaminants from the unreacted substrates, the red-like result was repeatedly washed with deionized water and diethyl ether. The product was eventually vacuum-dried and used for the following steps.

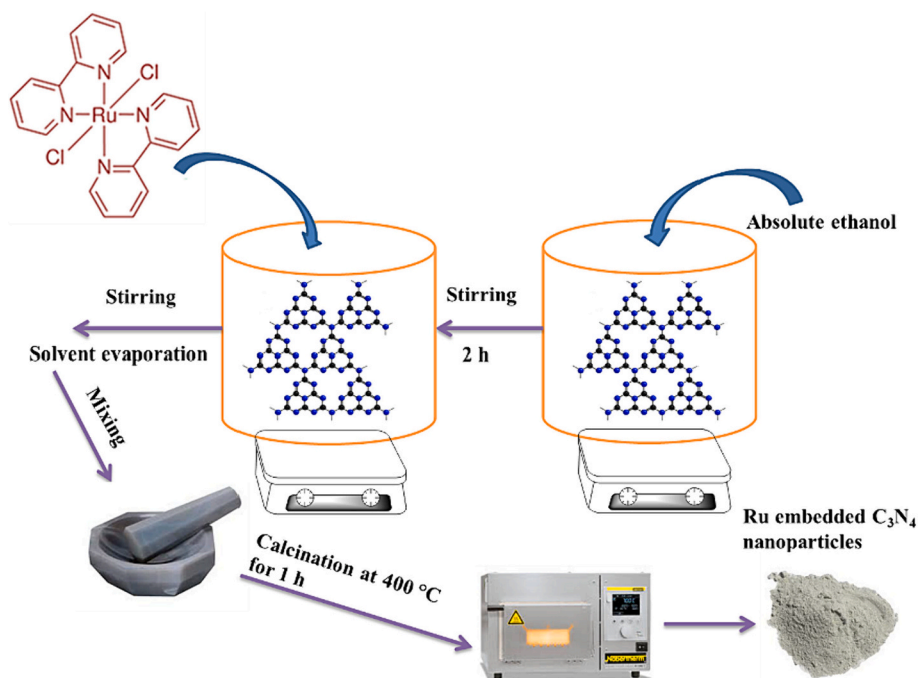### 2.2. Synthesis of bulk g-C$_3$N$_4$ photocatalysts

Melamine was employed as a precursor for the synthesis of g-C$_3$N$_4$ powder was placed in a covered alumina crucible and heated in a muffle furnace up to 520 °C in the air at the heating rate of 10 °C min^{-1} for 4 h. After the thermal treatment, the crucible was cooled down to room temperature, the resultant yellow products were collected and ground into powders using a mortar and pestle.

2.3. Synthesis of Ru/g-C$_3$N$_4$ photocatalysts

Ru/g-C$_3$N$_4$ photocatalysts were prepared by mixing g-C$_3$N$_4$ with an appropriate amount of [Ru(bpy)$_2$Cl$_2$]$^+$ for 2 h in ethanol solution (Scheme 1). The mixture was heated at 80 °C for 3 h. After solvent evaporation and drying, Ru/g-C$_3$N$_4$ photocatalysts were obtained at a calcination temperature of 400 °C for 1 h. The grey-like powder samples were collected and titled as follows: 0.5 % Ru/CN, 0.8 % Ru/CN, 1 % Ru/CN, and 2 % Ru/CN. According to Shimoyama et al. [59], the amount of RuO$_2$ in RuO$_2$/g-C$_3$N$_4$ was calculated using the inductively coupled plasma-optical emission spectroscopy (ICP-OES) system. Based on this technique, 1.0 wt% of RuCl$_3$·nH$_2$O has around 0.62 RuO$_2$, thus for the most active photocatalyst in this study that contains 0.8 % Ru-complex should be expected to have about 0.5 % RuO$_2$.

2.4. Characterization

X-ray diffraction (XRD) patterns of the prepared photocatalysts were conducted using PANalytical X'pert PRO theta-theta X-ray diffraction system with Cu Kα radiation (λ = 1.540598 nm). High-resolution transmission electron microscopy (HRTEM) images were taken on a JEM 2100F microscope operated at 200 kV, together with energy-dispersive X-ray spectroscopy (EDX) obtained from an attached Oxford Link EDX spectrometer. UV–vis absorption and diffuse reflection spectra (DRS) were measured using a UV–vis spectrophotometer (VARIAN Cary 4000) equipped with an integrating sphere attachment. The photo-luminescence (PL) spectra were obtained using a VARIAN Cary Eclipse Fluorescence Spectrophotometer at room temperature with excitation by incident light of 350 nm. X-ray photoelectron microscopy (XPS) was conducted in an ultra-high vacuum in a Thermo Scientific ESCALAB 250 Xi with Al Kα radiation as the excitation source ($h\nu$ = 1486.6 eV). To compensate surface charges effect, the binding energies were calibrated using C1s peak at 284.60 eV as the reference. The Brunauer-Emmett-Teller (BET) specific surface area of the photocatalysts was investigated by N$_2$ gas adsorption experiments equipped with a Tri Star II (Micrometrics). The Fourier transform infrared (FT-IR) spectra were captured using a Bruker FT-IR Tensor 27 spectrometer with platinum ATR in the wavenumber range of 400–4000 cm^{-1}. Electrochemical experiments including electrode preparations, and electrochemical

Scheme 1. Synthesis outline of Ru/g-C$_3$N$_4$ photocatalysts

parameters were investigated according to Ismael et al. [19].

2.5. Photocatalytic hydrogen production test

The photocatalytic hydrogen production reaction was carried out in a typical double-wall-inner irradiation-type quartz reactor connected to a glass-closed gas system, using a 500 W Hg mid-pressure immersion lamp as the light source. The photocatalyst (0.5 g) was loaded with 0.5 wt% Pt by in situ photodeposition method using H$_2$PtCl$_6$ as the precursor and dispersed in an aqueous solution (500 mL) containing methanol (10 %) as a hole scavenger (sacrificial electron donor). The reaction solution was degassed under flowing Argon gas with the flow of 50 N mL min^{-1} for 20 min to remove air completely, before starting the H$_2$ evolution experiment, the reaction solution was cooled with double-wall quartz using a thermostat (LAUDA). The amount of evolved hydrogen was analyzed using a multichannel analyzer (Emerson) equipped with a thermal conductivity detector.

3. Results and discussion

3.1. XRD analysis

The crystal and phase structures of the pure g-C$_3$N$_4$ and different Ru-embedded g-C$_3$N$_4$ photocatalysts were characterized by X-ray diffraction (XRD) analysis and the results are shown in Fig. 1. The weak diffraction peak was located at 13°, which can be indexed as (100) crystal planes, while the strong diffraction peak positioned at 27.3° is the (002) crystal plane of g-C$_3$N$_4$. The former is ascribed to the interlayer-stacking peak of the aromatic system and the latter corresponds to the interplanar structural packing motif of g-C$_3$N$_4$ [60]. Furthermore, in the XRD patterns of g-C$_3$N$_4$, there were no discernible melamine diffraction peaks, indicating that the precursors were fully transformed into the g-C$_3$N$_4$ structure during calcination. Importantly, weak signals at 35.2° and 43.9° appear in the spectra of Ru-embedded g-C$_3$N$_4$ samples, corresponding to the (101) planes of rutile RuO$_2$ and metal ruthenium (Ru^0), respectively. Similarly, the intensity of these peaks is also weak, which could be due to good dispersion or small particle sizes of ruthenium metal on the support [61]. This reveals that
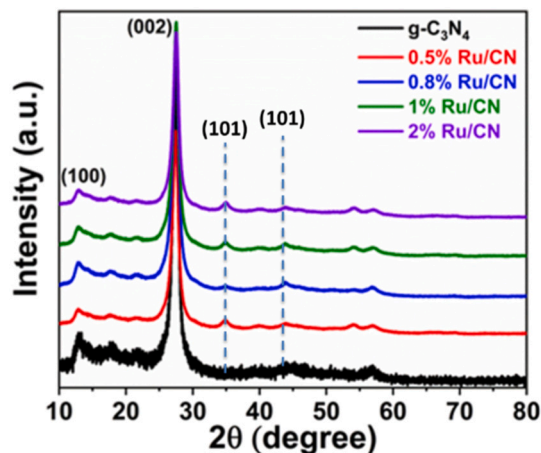
Fig. 1. XRD patterns of pure g-C$_3$N$_4$ and different Ru/g-C$_3$N$_4$ photocatalysts.

the graphitic-like structure of g-C$_3$N$_4$ was retained after Ru loading. In contrast, the 0.8 % Ru/CN (the most active photocatalyst in this study) exhibits greater crystallinity, as evidenced by the higher peak intensity at (100) in comparison to others, confirming a reduction in particle size and enhancing the specific surface area as shown later. Most significantly, the absence of any additional impurity peaks in any of the samples indicates that the crystal structure remained unaltered during the melamine-assisted synthesis of g-C$_3$N$_4$. The same XRD structural behavior was reported by Tahir et al. in the synthesis of Ru-embedded 3D g-C$_3$N$_4$ hollow nanosheets for photocatalytic hydrogen production [62]. In other studies, the absence of Ru peaks in the Ru-embedded g-C$_3$N$_4$ also can be ascribed to the low amount of Ru, smaller size, and a high dispersion degree of Ru nanoparticles over g-C$_3$N$_4$. The same observations were reported for Ru/g-C$_3$N$_4$ porous and Ru/g-C$_3$N$_{4-x}$ photocatalysts described by Li et al., and Yang et al., respectively [52,63]. Furthermore, Ru-based dye was previously combined with g-C$_3$N$_4$, but no Ru peaks were discovered [64]. On the other hand, a defect structure was observed in the Ru-supported g-C$_3$N$_4$ prepared by Li et al. [65], which may be attributed to the induction of Ru atoms that affected the

development of g-C_3N_4 molecular chains during the synthesis process and changed the bonding mode of part of C and N in the skeleton of g-C_3N_4. This result is in good agreement with the following TEM and XPS results.

3.2. FT-IR analysis

FT-IR spectra were investigated to determine the molecular structure of the pure g-C_3N_4 and 0.8 % Ru/CN photocatalysts. As illustrated in Fig. 2, the sharp characteristic peak observed at 810 cm^{-1} stemmed from the breathing mode of the *s*-triazine ring which normally appeared as a typical peak in the g-C_3N_4 structure [66]. The prominent bands in the region of 1248–1624 cm^{-1} were assigned to a typical stretching vibration of aromatic C–N in the graphite-like structure of carbon nitride [67]. The broad peak at around 3100 cm^{-1} could be attributed to the stretching vibrational modes of residual –NH–, NH$_2$ components associated with uncondensed amino groups in the structure of g-C_3N_4 and to O–H from atmospheric absorbed water [68]. Additionally, there is no discernible difference in the spectra of pure g-C_3N_4 and Ru-embedded g-C_3N_4, demonstrating that Ru loading does not affect the structural properties of g-C_3N_4. The same results were reported for Ru/g-C_3N_4 described by Sharma and her team [55]. The retention of the g-C_3N_4 structure following ruthenium loading is indicated by the similarities between the FT-IR spectra of the Ru/g-C_3N_4 catalysts and the g-C_3N_4 supports. Additionally, as established in the literature [69], it implies a non-covalently linked interaction between g-C_3N_4 and metal nanoparticles in the catalysts (Table 1).

3.3. TEM and HRTEM analysis

Fig. 3a–c presents the transmission electron microscopy (TEM) images of bulk g-C_3N_4 and the most active photocatalysts (0.8 % Ru/CN). As shown in Fig. 3a, pure g-C_3N_4 exhibits thin and large sheets without any porosity. Furthermore, for the most active photocatalyst (0.8 % Ru/CN), TEM images revealed an almost similar pattern of thin sheet structure of g-C_3N_4 loaded with the darker spotted area (marked in red for ruthenium and blue for platinum), corresponding to the presence of both ruthenium and platinum nanoparticles over the g-C_3N_4 sheet (Fig. 3b & c). Platinum nanoparticles were added to the photocatalytic reaction through in situ deposition and used as a cocatalyst to enhance the hydrogen production activity. Obviously, smaller, and different sizes
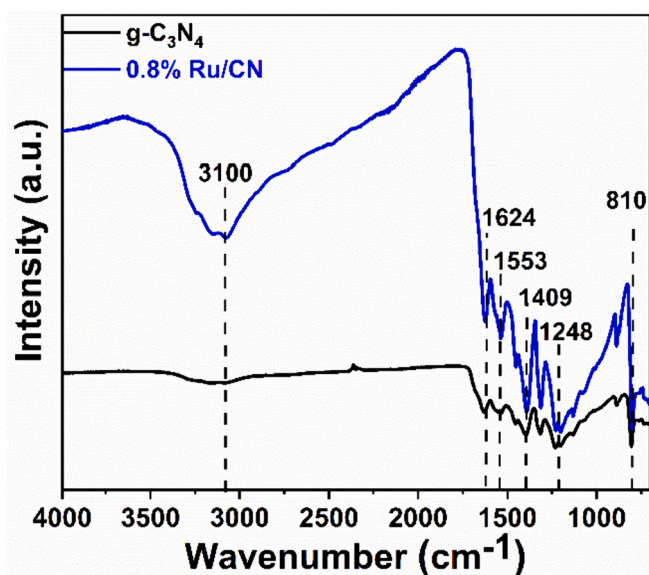

Fig. 2. FT-IR absorption spectra of pure g-C_3N_4 and 0.8 % Ru/g-C_3N_4 photocatalysts.

Table 1

summarizes the stretching vibration and the specific functional groups in the g-C_3N_4 structure with the corresponding wavenumbers and literature.

Photocatalysts	Frequency peak value or wavenumbers (cm^{-1})	Stretching vibration and specific functional group	References
0.8 % Ru/CN, and g-C_3N_4	810	S-triazine ring in g-C_3N_4 structure	64
0.8 % Ru/CN, and g-C_3N_4	1248–1624	Aromatic C–N in the graphite-like structure of	65
0.8 % Ru/CN, and g-C_3N_4	3100	Residual –NH–, NH$_2$ components, and O–H from atmospheric absorbed water	66

of Ru are uniformly dispersed over the entire g-C_3N_4 surface and similar results were obtained during the corresponding EDX spectra (Fig. 3d). Previously, Ru nanoparticles were loaded over g-C_3N_4 and reported very small Ru nanoparticles distributed over nanosheets [52]. On the other hand, EDX spectra were applied to determine the presence of the elements on the photocatalyst. Fig. 3d & e showed that carbon (C), nitrogen (N), oxygen (O), ruthenium (Ru), and platinum (Pt) are the only elements in the two spectra. Fig. 3d presents the existence of ruthenium nanoparticles marked by the red square in Fig. 3b. On the other hand, Fig. 2e represents the existence of platinum marked by the blue square in Fig. 2c, carbon, nitrogen, and oxygen elements are related to the graphitic carbon nitride. The TEM and the EDX analysis of the most active photocatalyst confirmed the successful loading of Ru on the surface of the g-C_3N_4 which is inconsistent with the XPS discussed later.

3.4. N$_2$ adsorption/desorption isotherm and surface area analysis

The BET surface areas of the different Ru-embedded g-C_3N_4 photocatalysts and pure g-C_3N_4 were investigated by N$_2$ adsorption/desorption isotherms. Fig. 4 displays the nitrogen adsorption/desorption isotherms for all photocatalysts. All the samples exhibit type IV isotherms (Brunauer-Deming-Deming-Teller (BDDT) classification), indicating the presence of well-defined mesopores [70]. These isotherms present an H3-type hysteresis loop, indicating the presence of slit-like pores, derived from the presence of aggregates [71]. All Ru/CN photocatalysts have larger surface areas than pure g-C_3N_4, indicating that the Ru ion contributes to the graphitic carbon nitride's increased surface area, which is beneficial for increasing photocatalytic hydrogen production. The increased activity of the Ru-embedded g-C_3N_4 is explained by the fact that, in general, a larger surface area can provide more sites for metal anchoring, increasing metal dispersity and, consequently, the catalytic activity of the photocatalyst [72].

3.5. XPS analysis

XPS was performed to analyze the chemical and valence states of the most active photocatalysts (0.8 % Ru/CN). As shown in Fig. 5a, the survey spectra of the photocatalyst before adding Pt nanoparticles show that the sample contains N, C, Ru, and a trace amount of O, which confirms the successful loading of Ru onto g-C_3N_4 in agreement with the XRD results. The peaks of O1s might initiate from O$_2$ or H$_2$O absorbed on the surface of g-C_3N_4. On the other hand, the survey spectra of the photocatalysts after the photocatalytic reaction (with Pt cocatalyst) are shown in Fig. 5b and observe the presence of Pt nanoparticles, which were used as a cocatalyst to enhance the photocatalytic performance. For the C 1s spectra partially overlapped by those of Ru 3d (Fig. 5c) and display the main core level peaks at 281.9, 284.8, 287.9, and 293.3 eV, which can be assigned to the Ru 3d$_{5/2}$ and external carbon contamination, the sp^2-bonded carbon to the three nitrogen atoms in the g-C_3N_4 lattice, and the π–π* excitation, respectively [73,74]. Furthermore, The

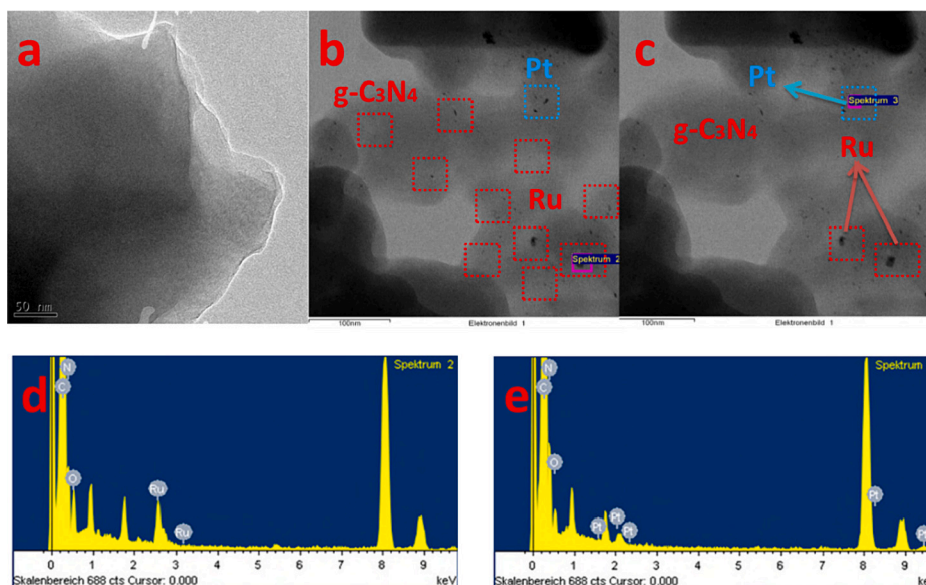**Fig. 3.** TEM images of pure g-C_3N_4 (a), the 0.8 % Ru/CN photocatalyst showing the presence of ruthenium and platinum (b & c), and the corresponding EDX spectra of the selected area (spectrum 2: for Ru) (d), and the corresponding EDX spectra of the selected area (spectrum 3: for Pt) (e) of 0.8 % Ru/CN photocatalyst.
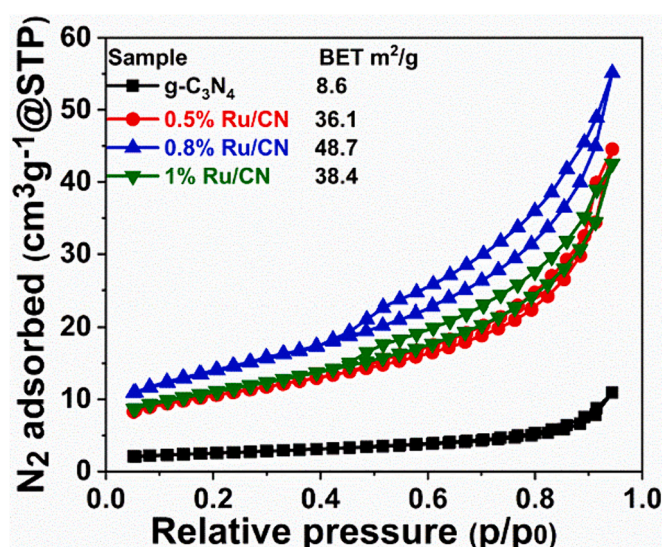

Fig. 4. N_2 adsorption-desorption isotherms of pure g-C_3N_4 and different Ru/g-C_3N_4 photocatalysts.

N 1s spectra (Fig. 5d) can be deconvoluted into four peaks at 398,1, 400, 401.2, and 404.2 eV. The first peak can be ascribed to sp^2 N involved in the triazine rings corresponding to C=N‒ C groups. The next two peaks can be attributed to the tertiary nitrogen (N‒ $(C)_3$), and terminal amino groups (C‒N‒H), respectively. The last one can be ascribed to the positive charge localization or charging effects of the π-excitation in the g-C_3N_4 structure [75,76]. The presence of amino groups in the final structure of g-C_3N_4 indicates that melamine was not fully condensed during the synthesis process, which fits with the previously reported [77,78]. For the Ru 3d XPS spectra (Fig. 5e), two peaks appeared at the binding energy of 284.1, and 280.3 eV which attributed to the Ru^0 $3d_{3/2}$, and Ru^0 $3d_{5/2}$, respectively, confirming the presence of metallic Ru^0 [79]. Meanwhile, two other peaks were observed at 285.1, and 281.4 eV which can be ascribed to Ru $3d_{3/2}$, and Ru $3d_{5/2}$ of RuO_2, respectively [80]. The synthesis of Ru^0 and RuO_2 was thought to be caused by the calcination of Ru precursor on carbon nitride at 300 °C in air. Similarly, the thermal breakdown of Ru and RuO_2 in the air was reported, with a combination of RuO_2 as the main phase and Ru detected in the sample calcined between 200 °C and 400 °C [81]. The organic substrate is most likely acting as a reductant [82]. In contrast, Tahir et al. prepared Ru-embedded 3D g-C_3N_4 hollow nanosheets without applying temperature and only RuO_2 without any metallic Ru^0 was observed [62]. Fig. 5f presents the XPS of the Ru 3p, which shows two peaks for the Ru $3p_{3/2}$ and Ru $3p_{1/2}$ spin-orbit state at BE values around 462.2 eV and 484.5 eV, indicating that Ru dominantly existed in the presence of Ru^0 species [83]. Thus, according to the XPS results, the Ru complex which was used as a precursor was decomposed to RuO_2 at 400 °C, and after contact with g-C_3N_4 which acts as a reductant, it reduced to Ru^0. In combination, XPS results confirm the presence of Ru on the g-C_3N_4 surface.

3.6. Optical properties

UV–vis diffuse reflectance spectroscopy (DRS) of the obtained photocatalysts is shown in Fig. 6. The photoabsorption edge of pure g-C_3N_4 is located at around 440 nm, indicating its bandgap of 2.87 eV (Fig. 6a) [84]. The absorption edges of Ru-loading g-C_3N_4 photocatalysts increased within the visible light region and red-shifted compared with the pure g-C_3N_4, accompanied by a change in the color of the sample from yellow to grey. Furthermore, the loading of g-C_3N_4 with Ru ions leads to the enhancement of the absorption ability in the visible light region, extending the absorption edge of a photocatalyst to 480 nm. It is worthwhile to note that the absorption tails in the wavelength range of 650–800 nm were increased with an increasing amount of ruthenium, which was ascribed to the internal d-d transition of Ru^{n+} and the excitation of an electron from one ruthenium ion to another on the neighboring cationic sites [85]. To learn more about how element doping affects samples, the bandgap (E_g) energies of all photocatalytic samples were estimated from the UV–vis absorption spectra by applying the Kubelka-Munk formula [86]. Therefore, the bandgaps energy can be estimated from the Tauc plots (Fig. 6b) and were 2.87, 2.8, 2.76, 2.6, 2.52, and 1.68 eV, for pure g-C_3N_4, 0.5 % Ru/CN, 0.8 % Ru/CN, 1 % Ru/CN, 2 % Ru/CN, and Ru(bpy)$_2$Cl$_2$.2H$_2$O, respectively. The results imply that the loading of g-C_3N_4 with Ru ion improves the visible-light activity of g-C_3N_4 by narrowing the bandgap energy. This result agrees with that reported for heteroatom loading g-C_3N_4 such as Fe [87], B [88], I [89], and P [90].
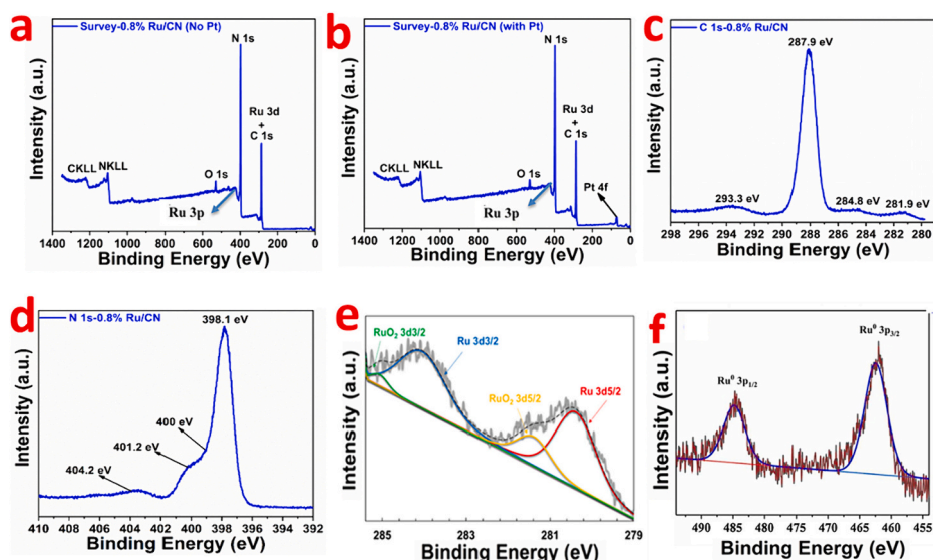
Fig. 5. XPS survey spectra of 0.8 % Ru/CN photocatalyst before (a) and after (b) the photocatalytic reaction, core level XPS spectra of C 1s (c), N 1s (d), Ru 3d (e), and Ru 3p (f) for 0.8 % Ru/CN photocatalyst.
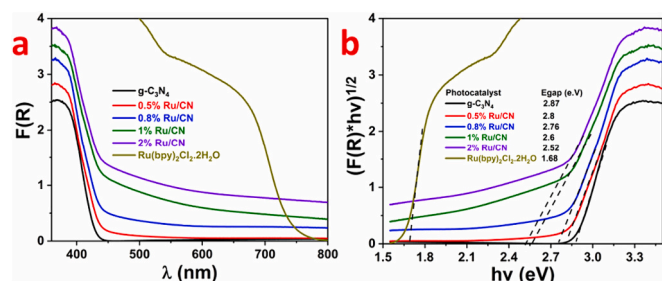

Fig. 6. Typical UV–vis absorption spectra (a), and Estimated bandgap energy employing Tauc plots of as prepared different Ru-embedded g-C_3N_4 compared to bare g-C_3N_4 and Ru-complex (b).

3.7. Mott-Schottky plots, photoluminescence, photocurrent, and electrochemical impedance spectroscopy analysis

The flat band potential of the pure g-C_3N_4 and 0.8 % Ru/CN photocatalysts were analyzed by the Mott–Schottky plots. The Mott-Schottky plots measurements of the photocatalyst electrodes were carried out using a standard three-electrode cell system at the frequency of 1 kHz in the dark using the Mott-Schottky relationship: [91]. The linear regions of Mott–Schottky plots of pure g-C_3N_4 and 0.8 % Ru/CN photocatalysts (Fig. 7) have a positive slope, indicating that both are typical n-type semiconductors [92]. Based on these plots, the flat band potential of pure g-C_3N_4 and 0.8 % Ru/CN photocatalysts were determined to be −0.65, and −0.75 V eV (vs Ag/AgCl), respectively, and can be converted to the NHE using the conversion relation of $E_{NHE} = E_{Ag/AgCl} + 0.197$ [93] which is equivalent to the −0.45, and −0.55 V vs. NHE, respectively. It's known that the flat band potentials of n-type semiconductors are 0.1 V more negative than E_{fb} [94], resulting in CB edges at about −0.55 and −0.65 V for the pure g-C_3N_4 and 0.8 % Ru/CN photocatalysts, respectively. It's clearly shown in Fig. 7 that loading of ruthenium over g-C_3N_4 caused a negative shift of flat band potential, resulting in decreasing the charge recombination that is responsible for the enhancement of the photocatalytic performance of the photocatalyst [93]. By combing the results obtained from the Tauc-plot (Fig. 6) and the Mott-Schottky plots (Fig. 7), the valence band positions of pure g-C_3N_4 and 0.8 % Ru/CN photocatalysts were calculated using the following equation $Evb = Ecb + Eg$ [94], resulting in 2.32, and 2.11 V, respectively.

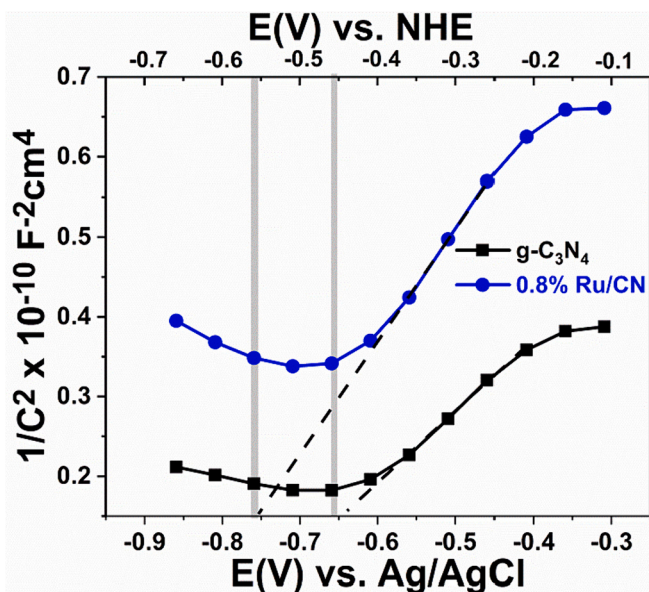**Fig. 7.** Mott-Schottky plot of pure g-C_3N_4 and 0.8 % Ru/CN film electrodes measured in the dark at the frequency of 1 kHz in an aqueous solution of Na_2SO_4 (0.1 M).

3.8. The origin of photoactivity enhancement of Ru/g-C_3N_4 photocatalysts

To verify the proposed mechanism, photoluminescence (PL) emission spectra and transient photocurrent (PC) were performed to study the charge recombination and transfer behavior of as-prepared photocatalysts. As shown in Fig. 8a, all samples displayed similar emission trends with a main emission peak centered at 460 nm, which is equivalent to the bandgap energy of pure g-C_3N_4 and can be assigned to the charge recombination in g-C_3N_4 [95]. The 0.8 % Ru/g-C_3N_4 photocatalyst presents the same peak with much lower intensity, indicating that the electron generated on the surface of g-C_3N_4 can be easily transferred to Ru, inhibiting charge recombination than that of pure g-C_3N_4. The data in Fig. 8b showed that the 0.8 % Ru/g-C_3N_4 has a much higher photocurrent density than the pure g-C_3N_4. The results can be
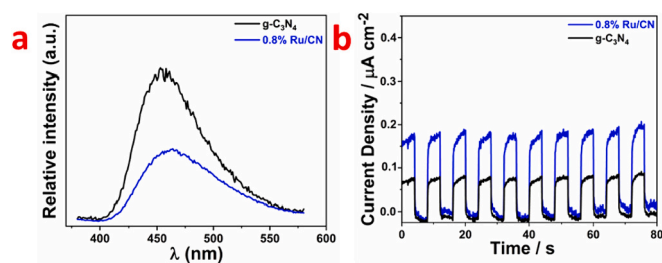
Fig. 8. Photoluminescence spectra excited at 320 nm (a), and transient photocurrent response (b) of pure g-C$_3$N$_4$ and 0.8 % Ru/CN electrodes.

implied by the fact that the 0.8 % Ru/CN photocatalyst can significantly boost the interfacial charge separation and transfer, which agrees with the enhancement of photocatalytic hydrogen production.

3.9. Photocatalytic hydrogen production of Ru/g-C$_3$N$_4$ photocatalysts

The photocatalytic activity of the different Ru/g-C$_3$N$_4$ photo-catalysts, as well as pure g-C$_3$N$_4$, was evaluated for photocatalytic H$_2$ evolution reaction under light irradiation of 500 W Hg lamp using methanol as a hole scavenger with and without Pt as a co-catalyst. Pure g-C$_3$N$_4$ has a hydrogen production activity in the absence (Fig. 9a) and presence (Fig. 9b) of Pt nanoparticles. However, its photocatalytic activity performance is lower compared to all Ru/g-C$_3$N$_4$ photocatalysts. When g-C$_3$N$_4$ is exposed to irradiation, the electrons are excited from the valence band to the conduction band. After that, these excited electrons are captured by the metallic Ru which can be used later for water

reduction. In the meantime, the VB hole can be transferred to RuO$_2$ and then hunted with methanol to produce H$_2$O and CO$_2$ (Fig. 8c). The same observations were reported by Wang et al. Their investigation showed that the presence of both metallic Ru^0 and RuO$_2$ is very beneficial for efficient ammonia synthesis [96]. Additionally, the photocatalytic activity of pure g-C$_3$N$_4$ and all Ru/g-C$_3$N$_4$ was further increased in the presence of Pt nanoparticles (Fig. 8b). It is known that Pt nanoparticles are outstanding inorganic co-catalysts and are commonly used to reduce the overpotential of water reduction. Pt nanoparticles were loaded via the in situ photodeposition method on the surface of g-C$_3$N$_4$ forming the Schottky barrier at the interface, which can promote the electron transfer from the CB of g-C$_3$N$_4$ to the Pt nanoparticles, facilitating the charge separation and further increase the photocatalytic hydrogen production (Fig. 8d) [97]. Among all Ru/g-C$_3$N$_4$ photocatalysts, 0.8 % Ru/CN exhibited the highest activity (246 μmol/h without Pt, and 1021 μmol/h with Pt). Further, an increase in the concentration of the Ru leads to a decrease in the photocatalytic activity, which is attributed to the shielding effect arising from the heavy Ru metal which acts as a recombination center [98]. Recently, Ismael [99] successfully synthesized Ru/TiO$_2$ via the precipitation method for determining hydrogen activity. Their finding revealed that the 0.1 % Ru-embedded TiO$_2$ photocatalyst was optimum and had the highest activity. Herein, the photocatalytic hydrogen activity of the Ru/g-C$_3$N$_4$ was assigned to the role of Ru in narrowing the bandgap energy and the role of both Ru and Pt in enhancing the charge separation at the interface. To investigate the stability of the photocatalyst after the reaction, XRD patterns were confirmed. As shown in Fig. 9e, similar diffraction peaks were seen in the XRD pattern of the recovered catalyst and the freshly generated catalyst (Fig. 9e), indicating that the catalyst's active metal sites
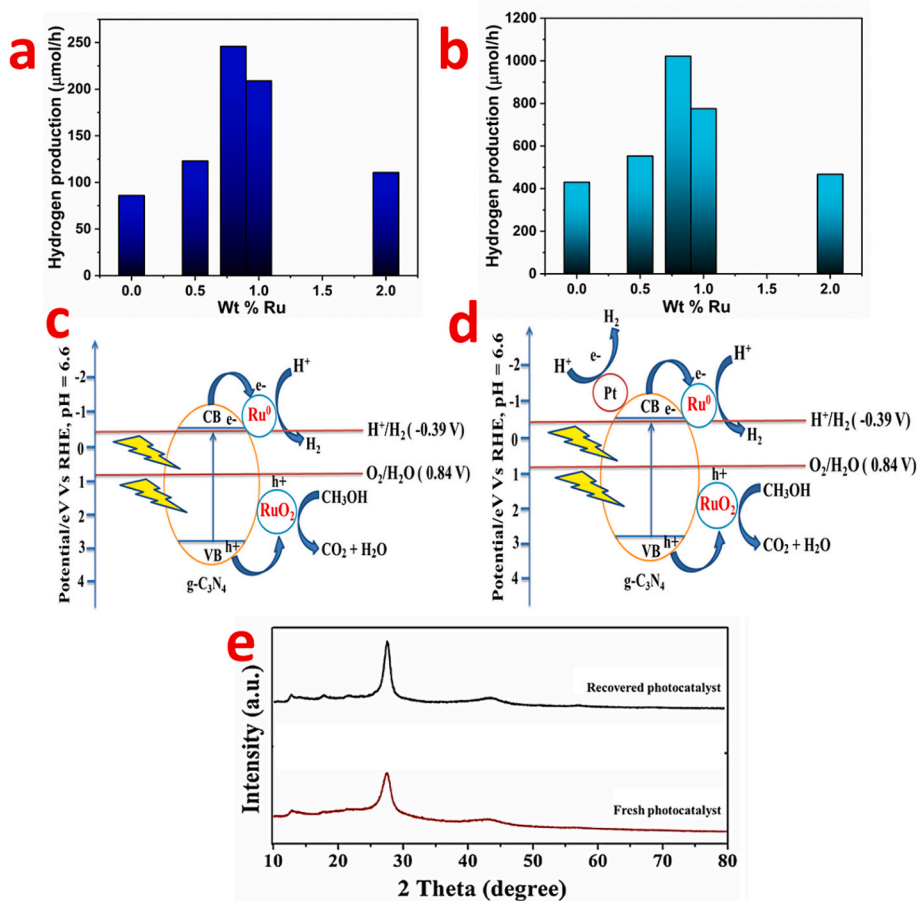

Fig. 9. Photocatalytic hydrogen production on pure g-C$_3$N$_4$ and different wt% Ru/CN without (a) and with Pt (b), the corresponding interfacial charge separation and reaction mechanism of Ru/CN photocatalyst without Pt (c), with Pt (d), and the stability test using XRD patterns (e).

exhibited exceptional stability during the hydrogen production reaction.

4. Conclusion

Novel Ru-embedded g-C₃N₄ photocatalysts were synthesized via a simple mixing method using Ru(bpy)₂Cl₂.2H₂O and melamine as the precursors of Ru and g-C₃N₄, respectively. 0.8 % Ru/CN revealed the highest hydrogen production activity under light irradiation in methanol solution with and without Pt nanoparticles. The higher activity of the Ru-embedded g-C₃N₄ compared to the pure g-C₃N₄ was attributed to the enlarged surface verified by the BET surface area experiment, and the role of Ru in enhancing the charge separation and transfer was proven by the photoluminescence (PL) and photocurrent (PC) experiments. In addition, the XPS results confirmed the existence of RuO₂ (Ru (II)) and metallic Ru (Ru⁰). Hence, the synthetic strategy to incorporate both Ru and RuO₂ to form in the photocatalytic system, where Ru acts as H₂ adsorption and activation sites for the reduction reaction and RuO₂ serves as fast hole extraction sites for the oxidation reaction, leads to the enhanced photocatalytic activity. Furthermore, Pt nanoparticles play a major role in increasing the hydrogen production rate over Ru-embedded photocatalysts. This study demonstrates a new low-cost synthesis method for the preparation of metal ion-embedded g-C₃N₄ for hydrogen evolution under light irradiation. This synthesis could be applied in the future for the synthesis of other metals embedded in g-C₃N₄ for different applications in photocatalysis.

CRediT authorship contribution statement

Mohammed Ismael: Writing – review & editing, Writing – original draft, Methodology, Investigation, Data curation, Conceptualization.

Declaration of competing interest

The authors declare that they have no known competing financial interests or personal relationships that could have appeared to influence the work reported in this paper.

Data availability

Data will be made available on request.

References

[1] S. Tasleem, M. Tahir, Current trends in strategies to improve photocatalytic performance of perovskites materials for solar to hydrogen production, Renew. Sustain. Energy Rev. 132 (2020) 110073.

[2] Z. Wang, B. Su, J. Xu, Y. Hou, Z. Ding, Direct Z-scheme ZnIn₂S₄/LaNiO₃ nanohybrid with enhanced photocatalytic performance for H2 evolution, Int. J. Hydrogen Energy 45 (7) (2020) 4113–4121.

[3] P.S. Shet, S. Shanmuga Priya, K. Sudhakar, M. Tahir, A review on current trends in potential use of metal-organic framework for hydrogen storage, Int. J. Hydrogen Energy 46 (21) (2021) 11782–11803.

[4] M. Ismael, Y. Wu, M. Wark, Photocatalytic activity of ZrO₂ composites with graphitic carbon nitride for hydrogen production under visible light, New J. Chem. 43 (2019) 4455–4462.

[5] M. Ismael, Enhanced photocatalytic hydrogen production and degradation of organic pollutants from Fe (III) doped TiO₂ nanoparticles, J. Environ. Chem. Eng. 8 (2020) 103676.

[6] M. Zheng, Y. Ding, L. Yu, X. Du, Y. Zhao, In situ grown pristine cobalt sulfide as bifunctional photocatalyst for hydrogen and oxygen evolution, Adv Func Mater. 27 (2017) 1605846.

[7] C. Pan, T. Takata, M. Nakabayashi, T. Matsumoto, N. Shibata, Y. Ikuhara, K. Domen, A complex perovskite-type oxynitride: the first photocatalyst for water splitting operable at up to 600 nm, Angew Chemie. 54 (2015) 2955–2959.

[8] M. Ismael, M. Wark, A simple sol–gel method for the synthesis of Pt co-catalyzed spinel-type CuFe₂O₄ for hydrogen production; the role of crystallinity and band gap energy, Fuel 359 (2024) 130429.

[9] M. Ismael, E. Elhaddad, M. Wark, Construction of SnO2/g-C3N4 composite photocatalyst with enhanced interfacial charge separation and high efficiency for hydrogen production and rhodamine degradation, Colloids Surf. A Physicochem. Eng. Asp. 638 (2022) 128288.

[10] M. Ismael, The photocatalytic performance of the ZnO/g-C₃N₄ composite photocatalyst toward degradation of organic pollutants and its inactivity toward

hydrogen evolution: the influence of light irradiation and charge transfer, Chem. Phys. Lett. 739 (2020) 136992.

[11] F.K. Kessler, Y. Zheng, D. Schwarz, C. Merschjann, W. Schnick, X. Wang, M. J. Bojdys, Functional carbon nitride materials—design strategies for electrochemical devices, Nat. Rev. Mater. 2 (17030) (2017) 1–17.

[12] H.A. Khayoon, M. Ismael, A. Al-Nayili, H.A. Alshamsi, Fabrication of LaFeO₃-nitrogen deficient g-C₃N₄ composite for enhanced the photocatalytic degradation of RhB under sunlight irradiation, Inorganic Chem Commun. 157 (2023) 111356.

[13] M. Ismael, Environmental remediation and sustainable energy generation via photocatalytic technology using rare earth metals modified g-C₃N₄: a review, J Alloys Compds. 931 (2023) 167469.

[14] M. Ismael, Photo-Fenton reaction enhanced visible-light activity of p-Photo-Fenton reaction enhanced visible-light activity of p-CuFe₂O₄/n-g-C₃N₄ heterojunction composites synthesized by a simple ultrasonic-assisted route for organic pollutants degradation, J Mater Res Bull. 151 (2022) 111803.

[15] M. Ismael, M. Wark, Photocatalytic activity of CoFe₂O₄/g-C₃N₄ nanocomposite toward degradation of different organic pollutants and their inactivity toward hydrogen production: the role of the conduction band position, FlatChem 32 (2022) 100337.

[16] Y.M. He, L.H. Zhang, M.H. Fan, X.X. Wang, M.L. Walbridge, Q.Y. Nong, Y. Wu, L. H. Zhao, Z-scheme SnO2−x/g-C₃N₄ composite as an efficient photocatalyst for dye degradation and photocatalytic CO₂ reduction, Sol. Energy Mat. Sol. C 137 (2015) 175–184.

[17] M. Ismael, Y. Wu, D.H. Taffa, P. Bottke, M. Wark, Graphitic carbon nitride synthesized by simple pyrolysis: role of precursor in photocatalytic hydrogen production, New J. Chem. 43 (2019) 6909.

[18] Y.J. Zhong, Z.Q. Wang, J.Y. Feng, S.C. Yan, H.T. Zhang, Z.S. Li, Z.G. Zou, Improvement in photocatalytic H₂ evolution over g-C₃N₄ prepared from protonated melamine, Appl. Surf. Sci. 295 (2014) 253–259.

[19] M. Ismael, Y. Wu, A facile synthesis method for fabrication of LaFeO₃/g-C₃N₄ nanocomposite as efficient visible-light-driven photocatalyst for photodegradation of RhB and 4-CP, New J. Chem. 43 (2019) 13783.

[20] M. Ismael, E. Elhaddad, D.H. Taffa, M. Wark, Solid state route for synthesis of YFeO₃/g-C₃N₄ composites and its visible light activity for degradation of organic pollutants, Catal. Today 313 (2018) 47–54.

[21] Y. Zhu, Y. Zhang, L. Cheng, M. Ismael, Z. Feng, Y. Wu, Novel application of g-C₃N₄/ NaNbO₃ composite for photocatalytic selective oxidation of biomass-derived HMF to FFCA under visible light irradiation, Adv Powder Technol. 31 (2020) 1148–1159.

[22] P.P. Singh, V. Srivastava, RSC Adv. 12 (2022) 18245–18265.

[23] G.H. Dong, W.K. Ho, C.Y. Wang, Recent advances in visible-light graphitic carbon nitride (g-C₃N₄) photocatalysts for chemical transformations, J. Mater. Chem. A 3 (2015) 23435–23441.

[24] H. Diarmand-Khalilabad, A. Habibi-Yangjeh, D. Seifzadeh, S. Asadzadeh-Khaneghah, E. Vesali-Kermani, g-C₃N₄ nanosheets decorated with carbon dots and CdS nanoparticles: novel nanocomposites with excellent nitrogen photofixation ability under simulated solar irradiation, Ceram. Int. 45 (2019) 2542–2555.

[25] M. Ismael, Facile synthesis of NiO-loaded g-C₃N₄ heterojunction photocatalyst for efficient photocatalytic degradation of 4-nitrophenol under visible light irradiation, J. Photochem. Photobiol. A Chem. 439 (2023) 114576.

[26] M. Ismael, One-step ultrasonic-assisted synthesis of Ni-doped g-C₃N₄ photocatalyst for enhanced photocatalytic hydrogen evolution, Inorganic Chem Commun. 151 (2023) 110607.

[27] D.X. Sun, Y.Y. Li, J. Zhou, H.C. Ma, Y. Wang, H.J. Zhu, Facile synthesis of high photocatalytic active porous g-C₃N₄ with ZnCl₂ template, J. Colloid Interf. Sci. 451 (2015) 108–116.

[28] W. Chen, M. Liu, X. Li, Synthesis of 3D mesoporous g-C₃N₄ for efficient overall water splitting under a Z-scheme photocatalytic system, Appl. Surf. Sci. 512 (2020) 145782.

[29] X. Wu, X. Wang, F. Wang, H. Yu, Soluble g-C₃N₄ nanosheets: facile synthesis and application in photocatalytic hydrogen evolution, Appl. Catal. Environ. 247 (2019) 70–77.

[30] X. She, H. Xu, Y. Xu, J. Yan, J. Xia, L. Xu, Y. Song, Y. Jiang, Q. Zhang, H. Li, Exfoliated graphene-like carbon nitride in organic solvents: enhanced photocatalytic activity and highly selective and sensitive sensor for the detection of trace amounts of Cu²⁺, J. Mater. Chem. A 2 (2014) 2563.

[31] N. Kumar, M. Kumari, M. Ismael, M. Tahir, R.K. Sharma, K. Kumari, J.R. Koduru, P. Singh, Graphitic carbon nitride (g–C₃N4)–assisted materials for the detection and remediation of hazardous gases and VOCs, Environ. Res. 231 (2023) 116149.

[32] Y. Zeng, X. Liu, C. Liu, L. Wang, Y. Xia, S. Zhang, S. Luo, Y. Pei, Scalable one-step production of porous oxygen-doped g-C₃N₄ nanorods with effective electron separation for excellent visible-light photocatalytic activity, Appl. Catal. B: Environ. 224 (2018) 1–9.

[33] J. Xu, Y. Qi, W. Wang, L. Wang, Montmorillonite-hybridized g-C₃N₄ composite modified by NiCoP cocatalyst for efficient visible-light-driven photocatalytic hydrogen evolution by dye-sensitization, Int. J. Hydrogen Energy 44 (2019) 4114–4122.

[34] X. Zhang, L. Yu, C. Zhuang, T. Peng, R. Li, X. Li, Highly asymmetric phthalocyanine as a sensitizer of graphitic carbon nitride for extremely efficient photocatalytic H₂ production under near-infrared light, ACS Catal. 4 (2014) 162.

[35] M. Ismael, A review on graphitic carbon nitride (g-C₃N₄) based nanocomposites: synthesis, categories, and their application in photocatalysis, J Alloys Compds. 846 (2020) 156446.

[36] Y. Yang, W. Guo, Y. Guo, Y. Zhao, X. Yuan, Y. Guo, Fabrication of Z-scheme plasmonic photocatalyst Ag@ AgBr/g-C₃N₄ with enhanced visible-light photocatalytic activity, J. Hazard. Mater. 271 (2014) 150.

[37] M. Ismael, Y. Wu, A mini-review on the synthesis and structural modification of g-C$_3$N$_4$-based materials, and their applications in solar energy conversion and environmental remediation, Sustain. Energy Fuels 3 (2019) 2907.

[38] S. Tonda, S. Kumar, S. Kandula, V. Shanker, Fe-doped and-mediated graphitic carbon nitride nanosheets for enhanced photocatalytic performance under natural sunlight, J. Mater. Chem. A 2 (2014) 6772.

[39] L. Jiang, X. Yuan, Y. Pan, J. Liang, G. Zeng, Z. Wu, H. Wang, Doping of graphitic carbon nitride for photocatalysis: a reveiw, Appl. Catal. Environ. 217 (2017) 388–406.

[40] Y. Kong, C. Lv, C. Zhang, G. Chen, Cyano group modified g-C$_3$N$_4$: molten salt method achievement and promoted photocatalytic nitrogen fixation activity, Appl. Surf. Sci. 515 (2020) 146009.

[41] S. Liang, Y. Xia, S. Zhu, S. Zheng, Y. He, J. Bi, M. Liu, L. Wu, Au and Pt co-loaded g-C$_3$N$_4$ nanosheets for enhanced photocatalytic hydrogen production under visible light irradiation, Appl. Surf. Sci. 354 (2015) 304–312.

[42] S. Samanta, Satyabadi Martha, Kulamani Parida, Facile synthesis of Au/g-C$_3$N$_4$ nanocomposites: an inorganic/organic hybrid plasmonic photocatalyst with enhanced hydrogen gas evolution under visible-light irradiation, ChemCatChem 6 (2014) 1453–1462.

[43] C. Ji, S.-N. Yin, S. Sun, S. Yang, An in situ mediator-free route to fabricate Cu$_2$O/g-C$_3$N$_4$ type-II heterojunctions for enhanced visible-light photocatalytic H$_2$ generation, Appl. Surf. Sci. 434 (2018) 1224–1231.

[44] M. Cao, K. Wang, I. Tudela, X. Fan, Synthesis of Zn doped g-C$_3$N$_4$ in KCl-ZnCl$_2$ molten salts: the temperature window for promoting the photocatalytic activity, Appl. Surf. Sci. 533 (2020) 147429.

[45] S. Meng, P. An, L. Chen, S. Sun, Z. Xie, M. Chen, D. Jiang, Integrating Ru-modulated CoP nanosheets binary co-catalyst with 2D g-C$_3$N$_4$ nanosheets for enhanced photocatalytic hydrogen evolution activity, J. Colloid Interface Sci. 585 (2021) 108–117.

[46] M.A. Abdel-Mageed, K. Wiese, M. Parlinska-Wojtan, J. Rabeah, A. Bruckner, J. R. Behm, Encapsulation of Ru nanoparticles: modifying the reactivity toward CO and CO$_2$ methanation on highly active Ru/TiO2 catalysts, Appl Catal B 270 (2020) 118846.

[47] M. Senthilnanthan, D.P. Ho, S. Vigneswaran, H.H. Ngo, M.K. Shon, Visible light responsive ruthenium-doped titanium dioxide for the removal of metsulfuron-methyl herbicie in aqueous phase, Sep. Purif. Technol. 75 (2010) 415–419.

[48] S. Lyu, Q. Cheng, Y. Liu, Y. Tian, T. Ding, Z. Jiang, J. Zhang, F. Gao, L. Dong, J. Bao, Q. Ma, H.Q. Yang, X. Li, Dopamine sacrificial coating strategy driving formation of highly active surface-exposed Ru sites on Ru/TiO2 catalysts in Fischer–Tropsch synthesis, Appl. Catal. Environ. 278 (2020) 119261.

[49] M. Tahir, Triphenylphosphine ruthenium (RuP) complex anchored with exfoliated g-C$_3$N$_4$ (ECN) with an externally reflected solar photoreactor system for highly efficient solar H$_2$ production, Chem. Eng. J. 471 (2023) 144551.

[50] J. Wang, J. Chen, P. Wang, J. Hou, C. Wang, Y. Ao, Robust photocatalytic hydrogen evolution over amorphous ruthenium phosphide quantum dots modified g-C$_3$N$_4$ nanosheet, J. Appl. Catal. B: Environ. 239 (2018) 578–585.

[51] M. Navlani-García, P. Verma, Y. Kuwahara, T. Kamegawa, K. Mori, H. Yamashita, Visible-light-enhanced catalytic activity of Ru nanoparticles over carbon modified g-C$_3$N$_4$, J. Photochem. Photobiol. A Chem. 358 (2018) 327–333.

[52] Yong-Ting Li, Shi-Hao Zhang, Guang-Ping Zheng, Pu Liu, Zhi-Kun Peng, Xiu-Cheng Zheng, Ultrafine Ru nanoparticles anchored to porous g-C$_3$N$_4$ as efficient catalysts for ammonia borane hydrolysis, Appl. Catal. Gen. 595 (2020) 117511.

[53] P. Sharma, Y. Sasson, Highly active Ru-g-C$_3$N$_4$ photocatalyst for visible light assisted selective hydrogen transfer reaction using hydrazine at room temperature, Catal. Commun. 102 (2017) 48–52.

[54] Q. Yang, T. Wang, Z. Zheng, C. Li, Constructing interfacial active sites in Ru/g-C$_3$N$_{4−x}$ photocatalyst for boosting H$_2$ evolution coupled with selective benzyl-alcohol oxidation, Appl. Catal. B: Environ. 315 (2022) 121575.

[55] P. Sharma, Y. Sasson, A photoactive catalyst Ru–gC$_3$N$_4$ for hydrogen transfer reaction of aldehydes and ketones, Green Chem. 19 (2017) 844–852.

[56] C. Tsounis, R. Kuriki, K. Shibata, J. Jhon, M. Vequizo, D. Lu, A. Yamakata, O. Ishitani, R. Amal, K. Maeda, Copolymerization approach to improving Ru(II)-complex/C$_3$N$_4$ hybrid photocatalysts for visible-light CO$_2$ reduction, ACS Sustainable Chem. Eng. 6 (11) (2018) 15333–15340.

[57] P. Kumar, C. Joshi, N. Labhsetwar, R. Boukherroub, S.L. Jain, A novel Ru/TiO2 hybrid nanocomposite catalyzed photoreduction of CO$_2$ to methanol under visible light, Nanoscale 7 (2015) 15258–15267.

[58] B.P. Sullivan, D.J. Salmon, T.J. Meyer, Inorg. Chem. 17 (1978) 3334–3341.

[59] X. Wang, L. Zhang, H. Lin, Q. Nong, Y. Wu, T. Wu, Y. He, Synthesis and characterization of a ZrO2/gC$_3$N$_4$ composite with enhanced visible-light photoactivity for rhodamine degradation, RSC Adv. 4 (2014) 40029–40035.

[60] M. Jafarpour, E. Rezapour, M. Ghahramaninezhad, A. Rezaeifard, A novel protocol for selective synthesis of monoclinic zirconia nanoparticles as a heterogeneous catalyst for condensation of 1,2-diamines with 1,2-dicarbonyl compounds, New J. Chem. 38 (2014) 676–682.

[61] M. Navlani-García, P. Verma, Y. Kuwahara, T. Kamegawa, K. Mori, H. Yamashita, A novel protocol for selective synthesis of monoclinic zirconia nanoparticles as a heterogeneous catalyst for condensation of 1,2-diamines with 1,2-dicarbonyl compounds, J. Photochem Photobiol. A 358 (2018) 327–333.

[62] B. Tahir, M. Tahir, M.G.M. Nawawai, A.H. Khoja, B.U. Haq, W. Farooq, Ru-embedded 3D g-C$_3$N$_4$ hollow nanosheets (3D CNHNS) with proficient charge transfer for stimulating photocatalytic H$_2$ production, Int. J. Hydrogen Energy 46 (2021) 27997–28010.

[63] Q. Yang, T. Wang, Z. Zheng, B. Xing, C. Li, Constructing interfacial active sites in Ru/g-C$_3$N$_{4−x}$ photocatalyst for boosting H$_2$ evolution coupled with selective benzyl-alcohol oxidation, Appl. Catal. Environ. 315 (2022) 121575.

[64] Y. Chen, Y. Liu, Z. Ma, Graphitic C$_3$N$_4$ modified by Ru (II)-based dyes for photocatalytic H$_2$ evolution, Colloids Surf. A Physicochem. Eng. Asp. 614 (2021) 126119.

[65] L. Li, Y. Yu, S. Lin, W. Chu, D. Sun, Q. Su, S. Ma, G. Du, B. Xu, Single ruthenium atom supported on g-C$_3$N$_4$ as an efficient photocatalyst for nitrogen fixation in ultra-pure water, Catal Commun. 153 (2021) 106294.

[66] J. Tang, J. Wang, L. Tang, Z. Xu, Y. Yi, H. Feng, J. Yu, X. Ren, Preparation of floating porous g-C$_3$N$_4$ photocatalyst via a facile one-pot method for efficient photocatalytic elimination of tetracycline under visible light irradiation, Chem Eng J 430 (2022) 132669.

[67] J. Enrique Samaniego-Benitez, K. Jimenez-Rangel, L. Lartundo-Rojas, A. García-García, A. Mantilla, Enhanced photocatalytic H$_2$ production over g-C$_3$N$_4$/NiS hybrid photocatalyst, Mater. Lett. 290 (2021) 129476.

[68] M.Q. Wang, W.H. Yang, H.H. Wang, C. Chen, Z.Y. Zhou, S.G. Sun, Pyrolyzed Fe–N–C composite as an efficient non-precious metal catalyst for oxygen reduction reaction in acidic medium, ACS Catal. 4 (2014) 3928–3936.

[69] B. Cai, Y. Zhang, J. Feng, C. Huang, T. Ma, H. Pan, Highly efficient g-C$_3$N$_4$ supported ruthenium catalysts for the catalytic transfer hydrogenation of levulinic acid to liquid fuel γ-valerolactone, Renew Energy 177 (2021) 652–662.

[70] J.Q. Xiang, G.J. Yu, B. Cheng, C.H. Ong, Microwave-hydrothermal preparation and visible-light photoactivity of plasmonic photocatalyst Ag-TiO2 nanocomposite hollow spheres, Chem. Asian J. 5 (2010) 1466.

[71] P. Niu, M. Qiao, Y. Li, L. Huang, T. Zhai, Distinctive defects engineering in graphitic carbon nitride for greatly extended visible light photocatalytic hydrogen evolution, Nano Energy 44 (2017) 73–81.

[72] H. Li, J. He, A. Riisager, S. Saravanamurugan, B. Song, S. Yang, et al., ACS Catal. 6 (2016) 7722–7727.

[73] H.J. Yan, Y. Chen, S.M. Xu, Synthesis of graphitic carbon nitride by directly heating sulfuric acid treated melamine for enhanced photocatalytic H$_2$ production from water under visible light, Int. J. Hydrogen Energy 37 (2012) 125–133.

[74] J. Liu, T. Zhang, Z. Wang, G. Dawson, W. Chen, Simple pyrolysis of urea into graphitic carbon nitride with recyclable adsorption and photocatalytic activity, J. Mater. Chem. 21 (2011) 14398–14401.

[75] S. Liu, S. Wang, Y. Jiang, Z. Zhao, G. Jiang, Z. Sun, Synthesis of Fe$_2$O$_3$ loaded porous g-C$_3$N$_4$ photocatalyst for photocatalytic reduction of dinitrogen to ammonia, Chem Eng J. 373 (2019) 572–579.

[76] F. Yang, V. Kuznietsov, M. Lublow, C. Merschjann, A. Steigert, J. Klar, A. Thomas, T. Schedel-Niedrig, Solar hydrogen evolution using metal-free photocatalytic polymeric carbon nitride/CuInS$_2$ composites as photocathodes, J. Mater. Chem. 1 (2013) 6407–6415.

[77] C.S. Yan, S.Z. Li, G.Z. Zou, Photodegradation of rhodamine B and methyl orange over boron-doped gC$_3$N$_4$ under visible light irradiation, Langmuir 26 (2010) 3894.

[78] J. Tang, J. Wang, L. Tang, C. Feng, X. Zhu, Y. Yi, H. Feng, J. Yu, X. Ren, Preparation of floating porous g-C$_3$N$_4$ photocatalyst via a facile one-pot method for efficient photocatalytic elimination of tetracycline under visible light irradiation, Chem. Eng. J. 430 (2022) 132669.

[79] X. Han, T. Si, Q. Liu, F. Zhu, R. Li, X. Chen, J. Liu, H. Sun, J. Zhao, Q. Zhang, H. Wang, 2D bimetallic RuNi alloy Co-catalysts remarkably enhanced the photocatalytic H2 evolution performance of g-C3N4 nanosheets, Chem. Eng. J. 426 (2021) 130824.

[80] Y. Feng, P. Huang, Z. Zhou, X. Ding, L. Liu, X. Liu, J. Kang, Negative differential resistance effect in Ru-based RRAM device fabricated by atomic layer deposition, Nanoscale Res. Lett. 14 (2019) 86.

[81] S. Musić, S. Popović, M. Maljković, K. Furić, A. Gajović, Influence of synthesis procedure on the formation of RuO$_2$, J. Mater. Sci. Lett. 21 (2002) 1131–1134.

[82] M.L. Green, M.E. Gross, L.E. Papa, K.J. Schnoes, D. Brasen, Chemical vapor deposition of ruthenium and ruthenium dioxide films, J. Electrochem. Soc. 132 (1985) 2677.

[83] K. Huang, C. Lin, G. Yu, P. Du, X. Xie, X. He, Z. Zheng, N. Sun, H. Tang, X. Li, M. Lei, H. Wu, Adv Funct Mater. 33 (2023) 2211102.

[84] Y. Wang, X. Wang, M. Antonietti, Polymeric graphitic carbon nitride as a heterogeneous organocatalyst: from photochemistry to multipurpose catalysis to sustainable chemistry, Angew. Chem. Int. Ed. 51 (2012) 68–89.

[85] P. Triggs, F. Levy, Optical and electrical properties of ruthenium-doped TiO$_2$, Phys. Status Solidi B 129 (1985) 363–374.

[86] L. Schwertmann, M. Wark, R. Marschall, Sol–gel synthesis of defect-pyrochlore structured CsTaWO$_6$ and the tribochemical influences on photocatalytic activity, RSC Adv. 3 (2013) 18908–18915.

[87] T. Tong, J. Zhang, B. Tian, F. Chen, D. He, Preparation of Fe^{3+}-doped TiO$_2$ catalysts by controlled hydrolysis of titanium alkoxide and study on their photocatalytic activity for methyl orange degradation, J. Hazard. Mater. 155 (2008) 572–579.

[88] Z. Lin, X. Wang, Angew., Nanostructure engineering and doping of conjugated carbon nitride semiconductors for hydrogen photosynthesis, Chem. Int. Ed. 52 (2013) 1735–1738.

[89] G. Zhang, M. Zhang, X. Ye, X. Qiu, S. Lin, X. Wang, Iodine modified carbon nitride semiconductors as visible light photocatalysts for hydrogen evolution, Adv. Mater. 26 (2014) 805–809.

[90] Z. Li, Q. Chen, Q. Lin, Y. Chen, X. Liao, H. Yu, C. Yu, Three-dimensional P-doped porous g-C$_3$N$_4$ nanosheets as an efficient metal-free photocatalyst for visible-light photocatalytic degradation of Rhodamine B model pollutant, J Taiwan Institute Chem Eng. 114 (2020) 249–262.

[91] W. Wu, S. Liang, L. Shen, Z. Ding, H. Zheng, W. Su, L. Wu, Preparation, characterization and enhanced visible light photocatalytic activities of polyaniline/Bi$_3$NbO$_7$ nanocomposites, J. Alloys Compd. 520 (2012) 213–219.

[92] L. Yu, X. Zhang, G. Li, Y. Cao, Y. Shao, D. Li, Highly efficient $Bi_2O_2CO_3/BiOCl$ photocatalyst based on heterojunction with enhanced dye-sensitization under visible light, Appl. Catal. Environ. 187 (2016) 301–309.

[93] H. Katsumata, Y. Tachi, T. Suzuki, S. Kaneko, Z-scheme photocatalytic hydrogen production over WO_3/gC_3N_4 composite photocatalysts, RSC Adv. 4 (2014) 21405–21409.

[94] J. Lim, D. Monllor-Satoca, J. Jang, S. Lee, W. Choi, Visible light photocatalysis of fullerol-complexed TiO_2 enhanced by Nb doping, Appl. Catal. Environ. 152–153 (2014) 233–240.

[95] P.F. Chen, P.X. Xing, Z.Q. Chen, X. Hu, H.J. Lin, L.H. Zhao, Y.M. He, In-situ synthesis of $AgNbO_3/g-C_3N_4$ photocatalyst via microwave heating method for efficiently photocatalytic H_2 generation, J. Colloid Interface Sci. 534 (2019) 163–171.

[96] H. Wang, X. Li, Q. Ruan, J. Tang, Ru and RuO_x decorated carbon nitride for efficient ammonia photosynthesis, Nanoscale 12 (2020) 12329–12335.

[97] G.J. Yu, F.L. Qi, M. Jaroniec, Hydrogen production by photocatalytic water splitting over Pt/TiO_2 nanosheets with exposed (001) facets, J. Phys. Chem. C 114 (2010) 13118.

[98] Y.M. He, L.H. Zhang, X.X. Wang, Y. Wu, H.J. Lin, L.H. Zhao, W.Z. Weng, H. L. Wang, M. Fan, Synthesis and characterization of a ZrO_2/gC_3N_4 composite with enhanced visible-light photoactivity for rhodamine degradation, RSC Adv. 4 (2014) 5905–5915.

[99] M. Ismael, Highly effective ruthenium-doped TiO_2 nanoparticles photocatalyst for visible-light-driven photocatalytic hydrogen production, New J. Chem. 43 (2019) 9596.